Noncontact Characterization of Carrier Mobility in Long-Wave Infrared HgCdTe Films With Terahertz Time-Domain Spectroscopy

Nils B. Refvik, Charles E. Jensen, David N. Purschke, Wenwu Pan, Howe R. J. Simpson, Wen Lei, Renjie Gu, Jarek Antoszewski, Gilberto A. Umana-Membreno, Lorenzo Faraone, and Frank A. Hegmann

***Abstract*—We use terahertz time-domain spectroscopy to measure the complex dielectric function of long-wave infrared $Hg_{1-x}Cd_xTe$ films ($x = 0.18, 0.20, 0.22$) as a function of temperature in a noncontact manner. Using a Drude–Lorentz model fit to the measured complex transmission function combined with a Kane model description of the band structure, we obtain the temperature-dependent conduction band carrier density, effective mass, scattering time, and carrier mobility for all three $Hg_{1-x}Cd_xTe$ films. The optical properties of a bare substrate of $Cd_{0.96}Zn_{0.04}Te$ were also measured in the terahertz region. The high quality of the $Hg_{1-x}Cd_xTe$ films is demonstrated by ultrahigh mobilities exceeding 10^5 $cm^2V^{-1}s^{-1}$ and ionized donor densities less than 3×10^{15} cm^{-3} at temperatures below 100 K.**

***Index Terms*—II–VI semiconductor materials, charge carrier processes, conductivity measurement, terahertz time-domain spectroscopy (THz-TDS).**

I. Introduction

MERCURY cadmium telluride ($Hg_{1-x}Cd_xTe$) is a widely tunable bandgap semiconductor with an extensive history as a premier infrared detection material [1], [2]. High-quality epitaxial films of $Hg_{1-x}Cd_xTe$ can be grown with continuous Cd fractions ranging from $x = 0$ to 1, corresponding to tunable bandgaps ranging from -0.3 eV (semimetal HgTe) to 1.5 eV (CdTe), covering most of the infrared spectra [1], [2]. At Cd fractions around $x = 0.20$, the band structure is highly nonparabolic with a bandgap on the order of 100 meV, which decreases as the material is cooled. This bandgap energy corresponds to the long-wave infrared regime. Additionally, the conduction band effective mass is very small ($m^* \sim 0.01m_e$, where m_e is the free electron mass) and decreases as the sample is cooled. Moreover, electron Hall mobilities in narrow-gap $Hg_{1-x}Cd_xTe$ ($x \sim 0.2$) can exceed 10^5 $cm^2V^{-1}s^{-1}$ with extremely long lifetimes, leading to excellent photodetector performance in the far infrared [1], [2].

Despite the extensive 60-year history and importance of $Hg_{1-x}Cd_xTe$ as a premium infrared material, there still remain challenges with quality control and noncontact characterization of carriers in epitaxially grown films [1], [3]. Beyond the Cd fraction and bandgap, which can be assessed through spectroscopic ellipsometry [4] and infrared transmission [5], noncontact characterization tools for assessing the free-carrier density, doping level, and mobility are important for optimizing the epitaxial growth process as well as device fabrication and performance.

Microwave reflectivity measurements [6], [7], along with far-infrared spectroscopy [3], [8], [9], are two potential noncontact characterization techniques of $Hg_{1-x}Cd_xTe$ films. However, microwave measurements have limited spectral resolution and have a large free-space wavelength (100 GHz–3 mm) limiting the spatial resolution attainable. The far-infrared spectroscopy is widely used for studying band-to-band transitions and vibrational structure in $Hg_{1-x}Cd_xTe$ [10], [11], [12]. Typically, in these measurements, the complex dielectric function must be inferred using the Kramers–Kronig relations because intensities are measured, rather than the amplitude and phase of the electric field.

Typical scattering rates of free carriers in high-mobility semiconductors lie in the few-terahertz (THz) range, which is near the limit of many far-infrared spectroscopy systems. For a semiconductor, such as $Hg_{1-x}Cd_xTe$ with mobility $\mu = 10^5$ $cm^2V^{-1}s^{-1}$ and effective mass $m^* = 0.01m_e$, the corresponding carrier scattering rate in the Drude model is $\Gamma = e/(\mu m^*) = 1.8$ THz. It is in this few-THz frequency range that optical probes will see significant dispersion in the optical conductivity and free-carrier absorption.

Manuscript received 24 January 2024; revised 26 March 2024; accepted 16 April 2024. Date of publication 25 April 2024; date of current version 5 July 2024. This work was supported in part by the Natural Sciences and Engineering Research Council of Canada, in part by the Canada Foundation for Innovation, in part by the Alberta/Technical University of Munich International Graduate School for Hybrid Functional Materials, in part by Alberta Innovates, in part by Alberta Innovates Technology Futures Strategic Chairs Program, in part by Australian Research Council under Grant CE200100010 and Grant DP200103188, and in part by the WA Node of the Australian National Fabrication Facility. *(Corresponding author: Nils B. Refvik.)*

Nils B. Refvik, Charles E. Jensen, Howe R. J. Simpson, and Frank A. Hegmann are with the Department of Physics, University of Alberta, Edmonton, AB T6G 2E1, Canada (e-mail: refvik@ualberta.ca; cjensen@ualberta.ca; hsimpson@ualberta.ca; hegmann@ualberta.ca).

David N. Purschke is with the Joint Attosecond Science Laboratory, National Research Council of Canada and University of Ottawa, Ottawa, ON K1N 5A2, Canada (e-mail: dpurschk@uottawa.ca).

Wenwu Pan, Wen Lei, Renjie Gu, Jarek Antoszewski, Gilberto A. Umana-Membreno, and Lorenzo Faraone are with the ARC CoE on Transformative Meta-Optical Systems, Department of Electrical, Electronic and Computer Engineering, The University of Western Australia, Perth, WA 6009, Australia (e-mail: wenwu.pan@uwa.edu.au; wen.lei@uwa.edu.au; renjie.gu@uwa.edu.au; jarek.antoszewski@uwa.edu.au; gilberto.umanamembreno@uwa.edu.au; lorenzo.faraone@uwa.edu.au).

Color versions of one or more figures in this article are available at https://doi.org/10.1109/TTHZ.2024.3393627.

Digital Object Identifier 10.1109/TTHZ.2024.3393627

THz time-domain spectroscopy (THz-TDS), lying at the lowest frequency end of the far-infrared regime, but above microwave frequencies, has been established as a powerful broadband, noncontact probe of transport, and the complex dielectric function in a variety of materials [13]. THz spectroscopy presents several advantages over other noncontact probes of conductivity. With THz-TDS, the direct sampling of the THz electric field waveform in the time domain enables the direct observation of the complex conductivity spectrum, without the use of the Kramers–Kronig relations [13], [14]. With appropriate modeling, carrier densities and mobilities can be directly extracted from the conductivity spectrum. The smaller free-space wavelength (1 THz~300 μm) results in higher spatial resolution compared with microwave frequency probes. Importantly, because the electric field of a THz pulse can be measured in the time domain, time-resolved measurements of picosecond-scale photoconductivity dynamics and mobilities can be obtained in pump-probe experiments [13]. Other approaches that use external magnetic fields (e.g., THz cyclotron resonance and THz optical Hall effect) or ellipsometry configurations have also enabled the direct measurements of carrier mobilities and effective masses in other material systems [15], [16], [17], [18].

For $Hg_{1-x}Cd_xTe$, THz spectroscopy has been used to observe hot carrier cooling and a few-picosecond long buildup of photoconductivity after femtosecond optical pulse excitation in a $Hg_{0.8}Cd_{0.2}Te$ film [19], [20]. There is already interest in studying $Hg_{1-x}Cd_xTe$ films and structures at THz frequencies with other techniques. THz pulse generation in $Hg_{1-x}Cd_xTe$ films after femtosecond pulse photoexcitation has been previously reported [21], [22], [23]. Additionally, there is ongoing research into inducing stimulated emission at THz frequencies in $Hg_{1-x}Cd_xTe$ structures [24], [25], [26], [27], [28] and the use of narrow-gap $Hg_{1-x}Cd_xTe$ in THz detection [29], [30], [31].

However, the full potential of THz-TDS as a characterization tool has not yet been demonstrated for $Hg_{1-x}Cd_xTe$ beyond an initial room-temperature measurement [32]. To date, no temperature-dependent studies of transport using THz-TDS in $Hg_{1-x}Cd_xTe$ have been reported. Additionally, there is only one reported room-temperature THz-TDS measurement of the THz dielectric function of $Cd_{0.96}Zn_{0.04}Te$, a standard substrate for $Hg_{1-x}Cd_xTe$ films [33]. From an industrial perspective, where $Hg_{1-x}Cd_xTe$ growth quality can vary significantly due to substrate defects, dislocations, and Hg vacancies [1], the noncontact and nondestructive characterization of carrier mobility with THz-TDS could be invaluable for quality control of large wafers [34]. Moreover, with the recent use of a variety of broadband and monochromatic far-infrared sources to probe $Hg_{1-x}Cd_xTe$ structures and topological states [35], [36], [37], [38], [39], it is imperative that the THz dielectric function in this important material is well understood.

Here, we use THz-TDS to measure the temperature-dependent THz dielectric function of three $Hg_{1-x}Cd_xTe$ thin films grown by molecular beam epitaxy (MBE). We extract the measurements of transport and dielectric properties as a function of temperature from 25 to 295 K, revealing a conductivity dispersion with significant free-carrier absorption. Using a Drude model, along with a Kane model description of the band structure, we calculate background doping levels and very high carrier mobilities from the measured complex transmission function. Importantly, our analysis considers the nonparabolicity of the band structure in $Hg_{1-x}Cd_xTe$ when determining the effective mass and carrier mobility using Boltzmann transport theory. Additionally, we measure the temperature-dependent dielectric function of a bare $Cd_{0.96}Zn_{0.04}Te$ substrate. To the best of our knowledge, this is the first reported temperature-dependent measurement of the THz dielectric function and mobilities of $Hg_{1-x}Cd_xTe$ films and of $Cd_{0.96}Zn_{0.04}Te$ using THz-TDS. Our results indicate that THz-TDS, in combination with material models, can be used as a powerful characterization tool to probe the conduction band carrier density, doping density, and mobility of grown $Hg_{1-x}Cd_xTe$ films in a noncontact manner.

II. Experimental Details

A. $Hg_{1-x}Cd_xTe$ Films

In this study, we examined three long-wave infrared $Hg_{1-x}Cd_xTe$ films with differing Cd fractions of $x = 0.18$, $x = 0.20$, and $x = 0.22$. The 4–5-μm-thick $Hg_{1-x}Cd_xTe$ films with the target Cd fractions, as given in Table I, were grown by MBE on 10 mm $\times$ 10 mm $Cd_{0.96}Zn_{0.04}Te$ (211)B-oriented substrates by the Microelectronics Research Group at the University of Western Australia [1]. The 50% cutoff wavelengths at room temperature as measured by Fourier transform infrared (FTIR) spectroscopy and narrow X-ray diffraction full width at half maxima ($<$ 30 arc-sec, indicative of high-quality growth) are shown in Table I. The $Cd_{0.96}Zn_{0.04}Te$ substrates were purchased from JX Nippon Mining and Metals and are a standard material for the epitaxial growth of $Hg_{1-x}Cd_xTe$ due to excellent lattice matching [40]. For characterization with THz-TDS, a bare $Cd_{0.96}Zn_{0.04}Te$ wafer was measured as well. The measured thickness of the bare substrate was 827 ± 1 μm. Often, As-grown $Hg_{1-x}Cd_xTe$ exhibits p-type doping due to the presence of Hg vacancies [1]. To counter this, the films were annealed in Hg vapor to provide a low n-type doping. A 200 nm ZnS passivation layer, which is transparent to THz, was deposited on the $Hg_{1-x}Cd_xTe$ surfaces. The films were coated with a photoresist for protection during shipping, which was removed with high-purity acetone before measurements.

B. THz-TDS System

In this experiment, we use a transmission-mode THz-TDS system, as described previously [41], [42]. Briefly, optical pulses with $\lambda = 800$ nm and temporal width of $\sim$100 fs are generated by a mode-locked Ti-Sapphire oscillator and multipass amplifier system operating at a 1.04 kHz repetition rate. A portion of the beam is incident on a 1-mm-thick ZnTe [110] crystal, where THz pulses are generated by optical rectification with a 0.4–2.4 THz bandwidth [13]. The THz beam is then directed to a $\sim$1.5 mm diameter focus by a sequence of off-axis parabolic mirrors. The numerical aperture of the focusing parabolic mirror is $\sim$0.17, giving a depth of focus at 1 THz of $\sim$7 mm. The sample is

TABLE I
SAMPLE INFORMATION DETERMINED AFTER GROWTH

x	Film Thickness (μm)	XRD FWHM (arcsec)	50% Cutoff wavelength at T = 295 K (μm)	Calculated bandgap at T = 295 K [61] (meV)	Calculated bandgap at T = 77 K [61] (meV)
0.22	4.7	26	6.3	181	113
0.20	4.0	26	6.5	151	78
0.18	4.8	22	7.5	123	43

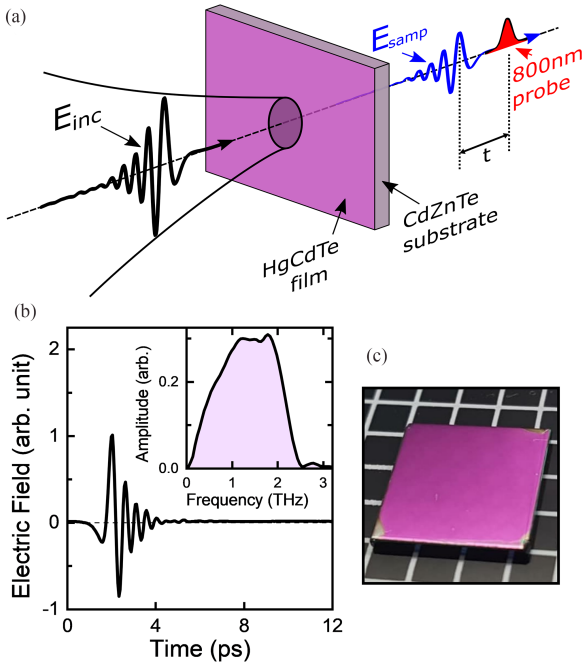

Fig. 1. (a) Schematic of the THz-TDS experiment. (b) Measured vacuum THz electric field and amplitude spectrum (inset) from the setup used in this work. (c) Photo of the grown 10 mm × 10 mm $Hg_{0.8}Cd_{0.2}Te$ film on $Cd_{0.96}Zn_{0.04}Te$ with a 200 nm ZnS passivation layer.

placed at the focus of the THz beam, and the resultant transmitted THz beam is collimated and then focused onto a second 1 mm ZnTe [110] crystal, where the THz electric field is measured in the time domain via electro-optic sampling with a second 800 nm probe pulse, as shown in Fig. 1(a). The measured THz waveform in vacuum and the amplitude spectrum are shown in Fig. 1(b). For each average THz waveform measurement, we take the mean of the Fourier transform amplitude and phases of all individual runs and use the standard deviation of the mean as the uncertainty. The sample mount was attached to a cold-finger cryostat, enabling measurements from room temperature down to 25 K. A silicon diode was attached to the sample mount near the samples to monitor the temperature. The setup was enclosed in a vacuum chamber at a pressure of 10^{-6} torr.

C. Dielectric Function Extraction

In THz-TDS, two THz field measurements are required to extract the complex index of refraction $\tilde{n} = n + ik$: the transmitted field through the sample of interest $E_{\text{samp}}(t)$ and a reference waveform $E_{\text{ref}}(t)$ with the sample removed. The sample transmission function is defined as the ratio of the Fourier transforms of the two electric field waveforms $\tilde{T}(\omega) = \tilde{E}_{\text{samp}}(\omega)/\tilde{E}_{\text{ref}}(\omega)$. In the case of the bare $Cd_{0.96}Zn_{0.04}Te$ substrate, which is a 0.827-mm-thick slab with relatively small absorption, the index of refraction can be analytically extracted from the measured transmission function [43], [44], yielding equations for the real and imaginary components. A material model for the complex dielectric function $\tilde{\epsilon}(\omega) = \tilde{n}^2$ can then be fitted to the measured $\tilde{n}$.

To extract the dielectric function of the 4–5-μm-thick $Hg_{1-x}Cd_xTe$ films, we can no longer use the direct index extraction method used for the thick $Cd_{0.96}Zn_{0.04}Te$ substrate, both due to high absorption and the small thickness of the $Hg_{1-x}Cd_xTe$ layer. Moreover, the Tinkham formula in the thin-film approximation [45], [46], which is often used in time-resolved THz spectroscopy experiments, cannot be used in this case. This is because the required conditions of $n\omega L/c \ll 1$ and $k\omega L/c \ll 1$, with L the sample thickness and c the speed of light, are not satisfied [44].

We instead model the full THz transmission function from vacuum through the multilayer system using a numerical scattering matrix approach [47]. We numerically calculate the total transmission function through the 200 nm ZnS [48] /4–5 μm $Hg_{1-x}Cd_xTe$ layers into the thick $Cd_{0.96}Zn_{0.04}Te$ substrate divided by a reference transmission function through the bare $Cd_{0.96}Zn_{0.04}Te$ substrate. This calculation takes as an input the complex index of refraction of each of the layers as well as the measured thicknesses of the layers. We then fit the model transmission function that includes the model $Hg_{1-x}Cd_xTe$ complex dielectric function to the measured transmission function ratio.

III. RESULTS AND DISCUSSION

Fig. 2(a) shows the measured THz waveform through vacuum, and the delayed waveform transmitted through the bare $Cd_{0.96}Zn_{0.04}Te$ substrate and the ZnS/$Hg_{0.8}Cd_{0.2}Te$/$Cd_{0.96}Zn_{0.04}Te$ system for three temperatures. The corresponding amplitude spectra normalized to the vacuum measurement are shown in Fig. 2(b). Qualitatively for the $Cd_{0.96}Zn_{0.04}Te$ transmission in Fig. 2(b), we observe broad attenuation over the THz bandwidth, which is attributed to a TO(Γ) phonon mode at 4.3 THz [43]. We also observe two resonances, one at 1.6 THz and one at 2.1 THz, attributed to a quasi-local ZnTe mode [49] and a summation 2TA(X) CdTe mode [43], respectively. This observation is consistent with a previous report of room-temperature THz-TDS on $Cd_{0.96}Zn_{0.04}Te$ [33]. With this knowledge, we fit the extracted complex index of the $Cd_{0.96}Zn_{0.04}Te$ substrate

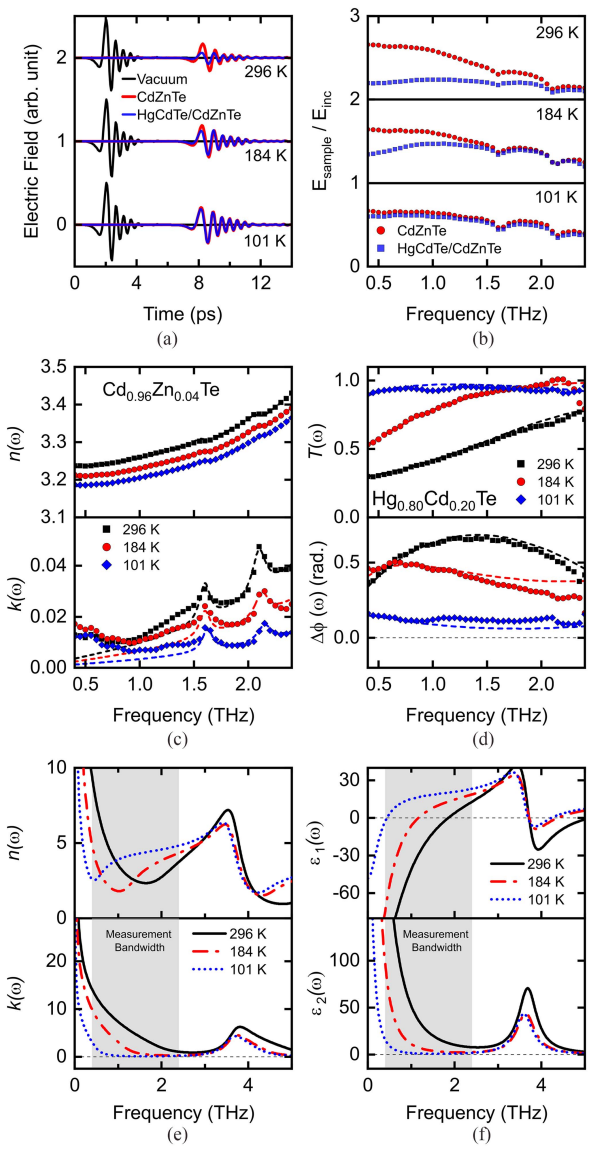

Fig. 2. (a) Time-domain measurements of the THz transmission through the bare $Cd_{0.96}Zn_{0.04}Te$ substrate (red), the $Hg_{0.8}Cd_{0.2}Te$ film (blue), and a vacuum reference (black) for three temperatures. (b) Corresponding amplitude spectra normalized with respect to the vacuum reference. (c) Extracted complex index of refraction of the bare $Cd_{0.96}Zn_{0.04}Te$ substrate for three temperatures and Lorentz oscillator model fits (dashed lines). (d) Amplitude $T(\omega)$ and phase difference $\Delta\phi(\omega)$ spectra of the $Hg_{0.8}Cd_{0.2}Te$ film (symbols) obtained by dividing the film + substrate transmission by the bare substrate transmission. The transmission model fits, which include the Drude–Lorentz model of the $Hg_{0.8}Cd_{0.2}Te$ conductivity, are shown by dashed lines. (e) Calculated complex index of refraction of the $Hg_{0.8}Cd_{0.2}Te$ film from the Drude–Lorentz fits for three temperatures. (f) Calculated complex dielectric function of the $Hg_{0.8}Cd_{0.2}Te$ film from the Drude–Lorentz fits for three temperatures. We indicate in (e) and (f) a shaded gray region corresponding to the 0.4–2.4 THz probe bandwidth and its location relative to the phonon mode at ~3.6 THz used in our model.

with three Lorentz oscillators

$$\tilde{\epsilon}(\omega) = \epsilon_1(\omega) + i\epsilon_2(\omega) = \epsilon_\infty + \sum_{j=1}^{3} \frac{S_j \omega_{0j}^2}{\omega_{0j}^2 - \omega^2 - i\omega\gamma_j} \quad (1)$$

where ϵ_∞ is the high-frequency dielectric background and S_j, ω_{0j}, and γ_j are the strength, resonant frequency, and damping rate of each mode, respectively. The index is then calculated as $\tilde{n} = \sqrt{\tilde{\epsilon}}$.

The extracted complex index (symbols) and Lorentz oscillator fits (dashed lines) for three temperatures are shown in Fig. 2(c). The fit parameters are listed in Table II. The real part n and the high frequencies of the imaginary part k are very well fit by the model. At low frequencies, there is an increase in k below 1 THz. Although the origin of this feature is unclear to us, a Drude model fit failed to yield physically reasonable parameters and, thus, we exclude background free-carrier conductivity as an explanation. We note that below 60 K, this feature was reduced in amplitude.

For the 4–5-μm-thick $Hg_{1-x}Cd_xTe$ films on $Cd_{0.96}Zn_{0.04}Te$, we observe the same resonances as the bare substrate at 1.6 and 2.1 THz, as shown in Fig. 2(b), for the $x = 0.20$ film. However, the transmission spectra normalized to the bare substrate in Fig. 2(d) are largely smoothed out. This indicates that the strong resonances primarily come from the underlying substrate rather than the $Hg_{1-x}Cd_xTe$ layer. Interestingly, we observe a small absorption feature close to 1 THz, which does not overlap with any substrate resonances, most easily seen in the 101 K measurement in Fig. 2(d). There was a previous debate in the literature about the origin of this feature seen in far-infrared spectroscopy [40]. We observed this absorption feature in all our samples at varying temperatures, supporting the interpretation of the feature being attributed to a disorder-induced TA phonon mode [40], [50]. Since the feature is relatively small, we do not include it in our overall fitting.

Overall, the dominant feature we observe in our bandwidth is large amplitude attenuation at high temperatures, which is most significant at low frequencies [see Fig. 2(d)]. We attribute this to free-carrier absorption from thermally generated intrinsic carriers. Because of the narrow bandgap, we expect a significant thermally generated intrinsic carrier density in the conduction band for $Hg_{1-x}Cd_xTe$ at room temperature [51]. This large carrier density will screen the transmission of the THz pulse through the film. As the sample is cooled below 100 K, the thermally generated intrinsic carrier density in $Hg_{0.8}Cd_{0.2}Te$ is expected to decrease by several orders of magnitude [51]. This has the effect of reducing the free-carrier absorption and, thus, increasing the THz transmission, which is what is observed in our measurements. We note that preliminary studies [20] show no evidence of nonlinear dynamics induced by the THz probe pulses.

In principle, the THz field transmission is reduced by the presence of both electrons and holes. However, due to the large effective mass and mobility difference between electrons and heavy holes in narrow-gap $Hg_{1-x}Cd_xTe$ ($\mu_e/\mu_{hh} \approx 100$) [2], the free-carrier absorption seen in our transmission measurements will be dominated by conduction band electrons. A similar situation arises in THz spectroscopy of other high-mobility semiconductors, such as GaAs and InSb [52], [53], [54]. Thus, we only include the contribution of conduction band electrons in our modeling of the THz conductivity.

In our fitting of the measured transmission function, we use the measured index of refraction of the $Cd_{0.96}Zn_{0.04}Te$ substrate

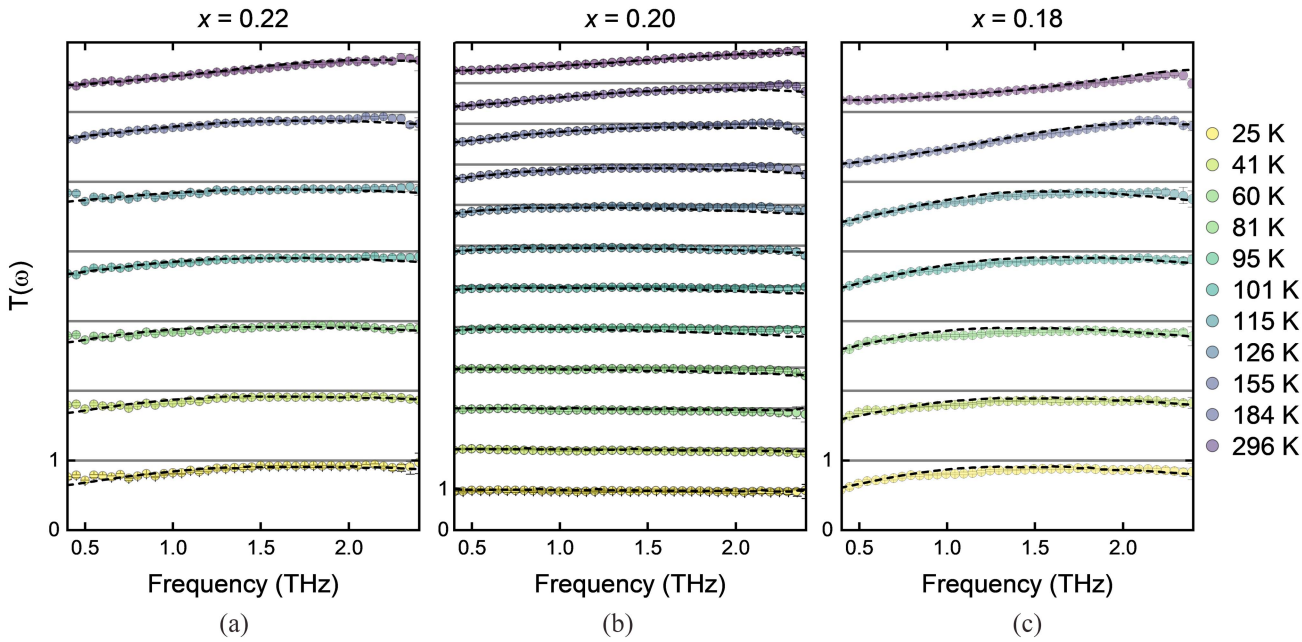

Fig. 3. Amplitude spectra $T(\omega)$ of the $Hg_{1-x}Cd_xTe$ films for (a) $x = 0.22$, (b) $x = 0.20$, and (c) $x = 0.18$, for all measured temperatures. The spectra are obtained, as shown in Fig. 2(d), by dividing the $Hg_{1-x}Cd_xTe$ + substrate transmission by the bare substrate transmission. The transmission model fits for each measurement are shown by the black dashed lines. The plots are offset for clarity.

TABLE II
FIT PARAMETERS FOR THE $Cd_{0.96}Zn_{0.04}Te$ SUBSTRATE

Temperature (K)	ϵ_{DC}	S_1	$\omega_{01}/2\pi$ (THz)	$\gamma_1/2\pi$ (THz)	S_2 ($\times 10^{-3}$)	$\omega_{02}/2\pi$ (THz)	$\gamma_2/2\pi$ (THz)	S_3 ($\times 10^{-3}$)	$\omega_{03}/2\pi$ (THz)	$\gamma_3/2\pi$ (THz)
25	10.00 ± 0.01	2.90 ± 0.01	4.44 ± 0.01	0.06 ± 0.04	2.5 ± 0.3	1.625	0.08 ± 0.04	1.1 ± 0.6	2.15	0.12 ± 0.05
41	10.00 ± 0.02	2.92 ± 0.02	4.12 ± 0.02	0.08 ± 0.02	3.7 ± 0.4	1.625	0.11 ± 0.03	2.3 ± 0.8	2.15	0.16 ± 0.01
60	10.02 ± 0.01	2.93 ± 0.01	4.27 ± 0.02	0.10 ± 0.03	4.5 ± 0.4	1.625	0.13 ± 0.02	2.5 ± 0.7	2.15	0.13 ± 0.09
81	10.02 ± 0.03	2.93 ± 0.02	4.17 ± 0.02	0.06 ± 0.04	3.6 ± 0.5	1.625	0.11 ± 0.01	4 ± 2	2.15	0.18 ± 0.01
95	10.03 ± 0.02	2.94 ± 0.02	4.22 ± 0.02	0.10 ± 0.02	59 ± 0.7	1.625	0.19 ± 0.04	3.7 ± 0.8	2.15	0.15 ± 0.01
101	10.10 ± 0.01	3.01 ± 0.01	4.33 ± 0.02	0.13 ± 0.07	4.1 ± 0.4	1.625	0.12 ± 0.09	2 ± 1	2.15	0.10 ± 0.03
115	10.08 ± 0.02	2.99 ± 0.02	4.23 ± 0.02	0.14 ± 0.06	6.2 ± 0.6	1.625	0.19 ± 0.01	2 ± 0.6	2.15	0.08 ± 0.03
126	10.10 ± 0.03	2.99 ± 0.03	4.33 ± 0.02	0.12 ± 0.06	4 ± 1	1.625	0.12 ± 0.09	5± 2	2.15	0.19 ± 0.08
155	10.15 ± 0.01	3.07 ± 0.01	4.28 ± 0.02	0.17 ± 0.03	1.8 ± 0.5	1.625	0.07 ± 0.04	2.1 ± 0.7	2.15	0.10 ± 0.03
184	10.25 ± 0.02	3.16 ± 0.02	4.32 ± 0.02	0.25 ± 0.04	4.7 ± 0.6	1.625	0.14 ± 0.03	3.6 ± 0.5	2.15	0.10 ± 0.02
224	10.27 ± 0.03	3.17 ± 0.03	4.27 ± 0.02	0.23 ± 0.02	7.8 ± 0.9	1.625	0.19 ± 0.05	5.2 ± 0.7	2.15	0.12 ± 0.02
296	10.44 ± 0.03	3.32 ± 0.02	4.41 ± 0.02	0.34 ± 0.04	9 ± 1	1.625	0.19 ± 0.08	6.6 ± 0.8	2.15	0.11 ± 0.02

and model the $Hg_{1-x}Cd_xTe$ equilibrium dielectric function using a Drude–Lorentz model, to account for free-carrier absorption and a single TO phonon mode located at approximately 3.6 THz [55]

$$\tilde{\epsilon}(\omega) = \epsilon_\infty + \frac{i\tilde{\sigma}(\omega)}{\epsilon_0\omega} + \frac{S\omega_0^2}{\omega_0^2 - \omega^2 - i\omega\gamma}. \quad (2)$$

Here, the free-carrier equilibrium conductivity $\tilde{\sigma}(\omega)$ is given by the Drude model in which we consider the contribution of conduction band electrons only

$$\tilde{\sigma}(\omega) = \frac{Ne^2\tau}{m^*}\frac{1}{1 - i\omega\tau} \quad (3)$$

where N is the conduction band electron density, τ is the scattering time, and m^* is the conduction band effective mass. The carrier mobility $\mu = e\tau/m^*$ can then be calculated.

As shown by infrared reflectivity studies, the optically active phonon spectrum in $Hg_{1-x}Cd_xTe$ is complex, with several additional modes above 3 THz [11], [56]. However, these modes cannot be directly observed within the THz bandwidth of our current setup. For simplicity of calculation and to effectively fit the Drude component in our bandwidth, we allow the Lorentz oscillator strength S to vary, while keeping a fixed damping rate of $\gamma = 0.5$ THz, a temperature-dependent central frequency ω_0 given in [55], and high-frequency dielectric function $\epsilon_\infty = 13.7$, similar to those measured in previous studies [40]. Improved characterization can likely be obtained in the future with a broader bandwidth THz-TDS system to directly measure the optical phonon spectra.

The transmission model with the Drude–Lorentz parameters was simultaneously fit to the measured complex transmission amplitude and phase for all three films at various temperatures. In particular, we performed measurements at 7 temperatures for the $x = 0.18$ and $x = 0.22$ films and 12 temperatures for the $x = 0.20$ film. Transmission model fits for the $x = 0.20$ film at three temperatures are shown in Fig. 2(d) and the fit parameters

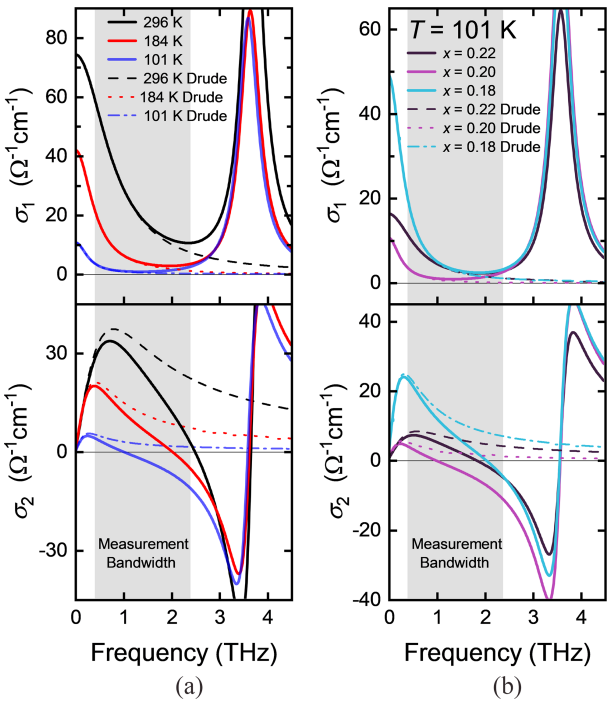

Fig. 4. (a) Total Drude–Lorentz complex optical conductivity spectra for three temperatures (solid lines) and the corresponding Drude contribution to the conductivity (dashed lines) for the $x = 0.20$ film. (b) Drude–Lorentz complex conductivity spectra (solid lines) for the three films at $T = 101$ K and the corresponding Drude contribution to the conductivity (dashed lines).

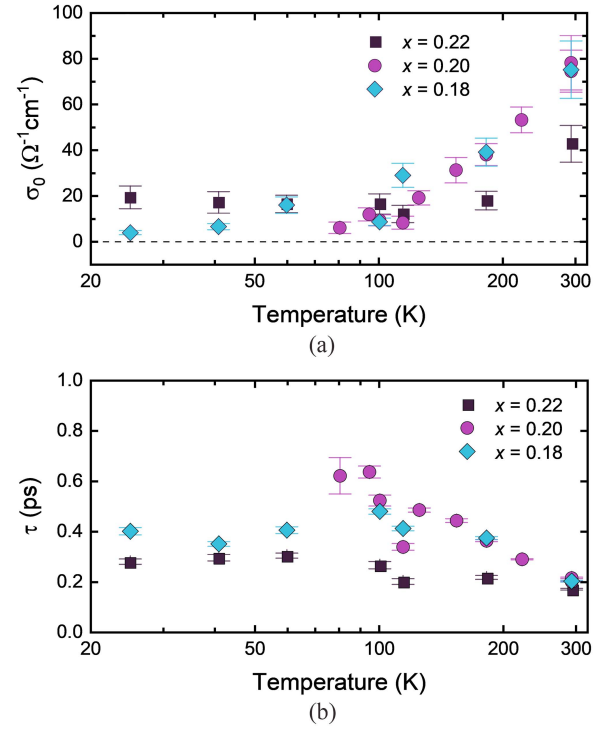

Fig. 5. (a) Extracted temperature-dependent dc Drude conductivity σ_0 and (b) momentum scattering time τ for the three $Hg_{1-x}Cd_xTe$ films.

for all measurements are recorded in Table III. Fig. 3 shows the measured transmission amplitude and model fits for all films at all temperatures. The transmission amplitude is very well fit by the model. Due to the small thickness of the $Hg_{1-x}Cd_xTe$ layers, the measured phase difference is very small with larger uncertainty in comparison with the transmission amplitude. Despite this, the model still reasonably captures the phase dispersion in the simultaneous fit, especially at low frequencies. Our simplifying model of the phonon spectrum outside the bandwidth likely accounts for the slight disagreement of the fit at higher frequencies. Additionally, in our fitting, we found a large variation (∼20%) in the Lorentz oscillator strength that did not significantly change the extracted Drude fit parameters, although the fit quality near the high-frequency end of the bandwidth was reduced. This indicates that the Drude component dominates the transmission amplitude spectrum, especially at lower frequencies.

Fig. 2(e) and (f) shows the corresponding calculated complex index of refraction and complex dielectric function, respectively, for those temperatures based on the extracted fit parameters. We indicate in the figure a shaded gray region indicating the 0.4–2.4 THz measurement bandwidth and its location relative to the location of the ∼3.6 THz phonon mode. The Drude–Lorentz contribution to the total complex conductivity at the three temperatures for the $x = 0.20$ film is shown as solid lines in Fig. 4(a). The Drude components are shown as broken lines. Additionally, we measured significant variation in the extracted conductivity across the three films, with a comparison at 101 K, as shown in Fig. 4(b). We see that the dominant component of $\sigma_1(\omega)$ in our bandwidth comes from the Drude conductivity, while both the Drude and Lorentz oscillator components contribute in $\sigma_2(\omega)$.

The extracted Drude dc conductivity, $\sigma_0 = Ne^2\tau/m^*$, and momentum scattering time τ are plotted in Fig. 5(a) and (b), respectively. As the temperature is reduced, all samples exhibit a reduction in the dc conductivity and an increase in the momentum scattering time. These two trends are consistent with an expected reduction of the intrinsic free-carrier population under cooling and a decreased carrier-phonon scattering rate with decreased temperature, respectively [57]. From these extracted parameters and a model for the band structure of $Hg_{1-x}Cd_xTe$, we can now proceed with a calculation of the temperature-dependent carrier density, effective mass, and carrier mobility for all three films.

Due to the high nonparabolicity of the band structure in narrow-gap $Hg_{1-x}Cd_xTe$, the effective mass m^* (shown as lines in Fig. 6(d) for three temperatures) varies from the known bottom-of-the-band value, m_0^*, for relatively small energies above the conduction band edge [50], [58], [59]. Near the conduction band edge, the nonparabolic band structure of $Hg_{1-x}Cd_xTe$ is well described by the Kane model [60]. The calculated conduction band from the Kane model near the band edge is shown in Fig. 6(a) for three temperatures for the $x = 0.20$ film. In the Kane model for energies near the conduction band edge, the effective mass is given by the relation $m^* = m_0^*(1 + 2E/E_g)$, where E is the energy measured with respect to the conduction band minimum, and E_g is the known temperature-dependent bandgap [shown in Fig. 7(a)] [61]. With

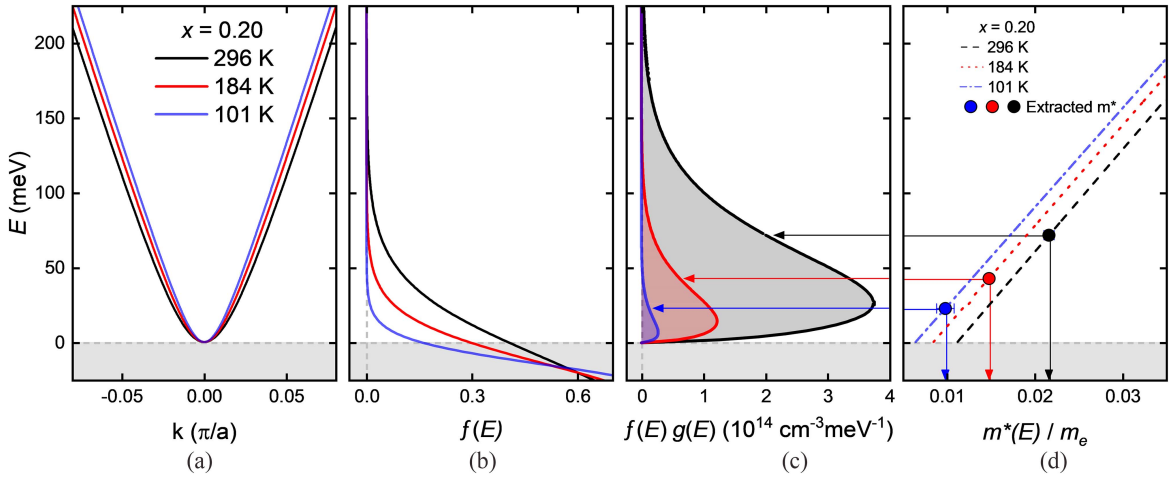

Fig. 6. (a) Calculated conduction band near $k = 0$ for three temperatures using the Kane model [60], [63]. E is defined with respect to the conduction band minimum. (b) Calculated Fermi–Dirac distribution $f(E, E_F, T)$ near the conduction band minimum using the extracted E_F from (4) for three temperatures. (c) Product of the Fermi–Dirac distribution from (b) and the density of states from (5) for three temperatures. (d) Energy-dependent Kane model effective mass (lines) given by $m^* = m_0^*(1 + 2E/E_g)$, and the extracted effective mass from the THz-TDS data at each temperature (symbols). The horizontal arrows indicate the corresponding energy for the extracted masses in the Kane model.

TABLE III
FIT PARAMETERS FOR THE $Hg_{1-x}Cd_xTe$ FILMS

	$x = 0.22$				$x = 0.20$				$x = 0.18$			
Temperature (K)	σ_0 (Ω^{-1}cm^{-1})	τ (fs)	S	$\omega_0/2\pi$ (THz) (Ref. [55])	σ_0 (Ω^{-1}cm^{-1})	τ (fs)	S	$\omega_0/2\pi$ (THz) (Ref. [55])	σ_0 (Ω^{-1}cm^{-1})	τ (fs)	S	$\omega_0/2\pi$ (THz) (Ref. [55])
25	19 ± 5	280 ± 10	3.6 ± 0.7	3.55	-	-	2.2 ± 0.3	3.55	3.8 ± 0.9	400 ± 10	6.0 ± 0.6	3.55
41	17 ± 5	290 ± 10	3.6 ± 0.6	3.57	-	-	2.7 ± 0.2	3.57	6 ± 1	350 ± 10	6.1 ± 0.5	3.57
60	16 ± 4	300 ± 10	3.9 ± 0.6	3.58	-	-	4.6 ± 0.6	3.58	16 ± 4	400 ± 10	6.9 ± 0.6	3.58
81	-	-	-	-	6 ± 3	620 ± 70	8.0 ± 0.3	3.59	-	-	-	-
95	-	-	-	-	12 ± 3	630 ± 20	10.0 ± 0.3	3.60	-	-	-	-
101	16 ± 4	260 ± 10	4.4 ± 0.6	3.60	9 ± 2	520 ± 20	2.9 ± 0.1	3.60	8 ± 1	480 ± 10	5.6 ± 0.4	3.60
115	12 ± 4	200 ± 10	4.3 ± 0.7	3.61	8 ± 3	330 ± 10	6.0 ± 0.1	3.61	29 ± 5	408 ± 9	9.8 ± 0.6	3.61
126	-	-	-	-	19 ± 3	481 ± 9	8.50 ± 0.3	3.61	-	-	-	-
155	-	-	-	-	31 ± 6	439 ± 1	11.4 ± 0.4	3.63	-	-	-	-
184	18 ± 4	212 ± 8	5.2 ± 0.7	3.64	38 ± 5	359 ± 4	6.2 ± 0.4	3.64	39 ± 6	370 ± 6	7.4 ± 0.7	3.64
224	-	-	-	-	53 ± 6	285 ± 2	10.1 ± 0.5	3.66	-	-	-	-
296	43 ± 8	166 ± 4	9.6 ± 0.9	3.69	74 ± 9	197 ± 2	10.8 ± 0.8	3.69	75 ± 10	198 ± 3	13 ± 1	3.69

this energy-dependent effective mass, the occupation of carriers in the conduction band must be considered.

To properly extract the carrier density and effective mass-dependent mobility simultaneously, we equate the THz-TDS measured dc conductivity $\sigma_0 = Ne\mu$ to the Kane model dc conductivity using the Boltzmann transport equation in the relaxation time approximation [58], [62]

$$\sigma_0 = -\frac{2e^2\tau}{3\pi^2\hbar^3}\sqrt{2m_0^*} \times \int_0^\infty \frac{[E\,(1+E/E_g)]^{3/2}}{1+2E/E_g}\frac{\partial f\,(E,E_F,T)}{\partial E}dE \quad (4)$$

where $f(E, E_F, T)$ is the Fermi–Dirac distribution with E_F the Fermi energy and T the lattice temperature. We first numerically solve for the Fermi energy E_F in (4). The resulting Fermi–Dirac distribution calculated using the extracted E_F for three temperatures in the $x = 0.20$ film is shown in Fig. 6(b). All the extracted Fermi energies for all three films were within 25 meV of the conduction band minimum. After determining the Fermi energy, we can then extract the carrier density (and thus the effective mass and mobility using the measured τ) using the density of states and carrier occupancy in the conduction band, $N = \int_0^\infty g(E)f(E, E_F, T)dE$. The nonparabolic density of states in the Kane model is given by [50]

$$g\,(E) = \frac{1}{2\pi^2}\left(\frac{2m_0^*}{\hbar^2}\right)^{3/2}\left(1+\frac{2E}{E_g}\right)\sqrt{E\left(1+\frac{E}{E_g}\right)}. \quad (5)$$

The resulting $f(E, E_F, T)g(E)$ product is shown in Fig. 6(c) for three temperatures. The area under the curves is decreasing with temperature, reflecting the expected decrease of thermally excited intrinsic carriers in the conduction band. For those same temperatures, the final extracted effective masses from the procedure are plotted as symbols on the $m^*(E)$ curves in Fig. 6(d). The horizontal arrows from these symbols indicate the corresponding energy above the conduction band edge in the Kane model for the given extracted masses.

The extracted temperature-dependent Drude carrier density, effective mass, and extracted carrier mobilities for all the films

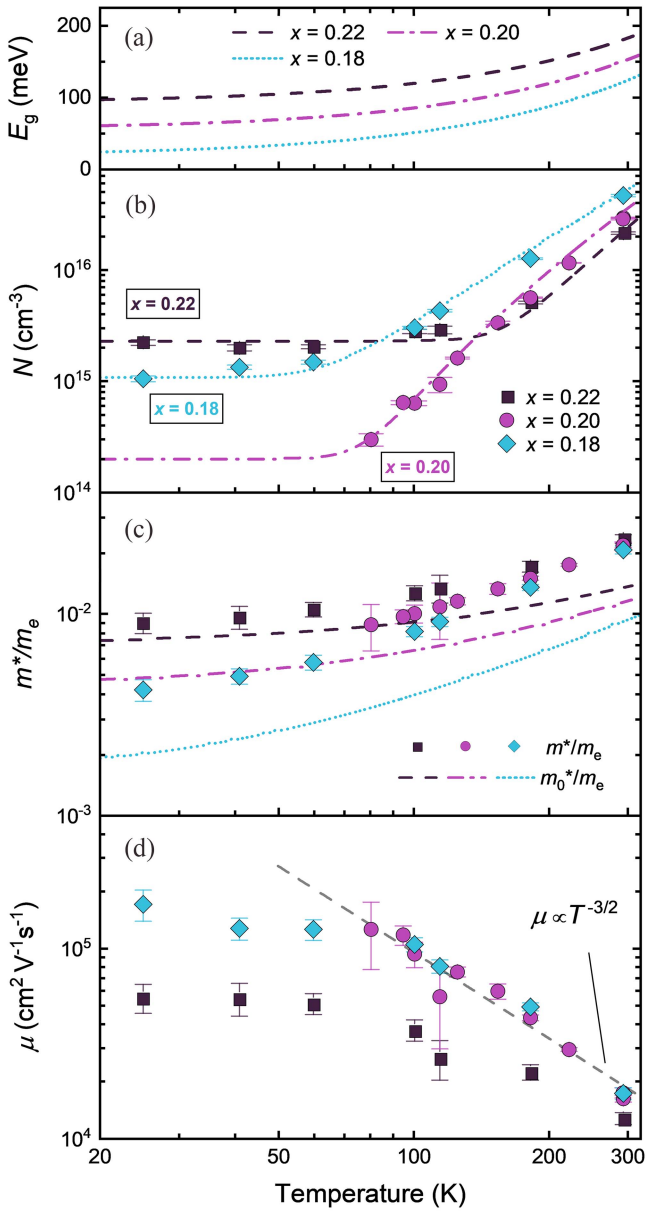

Fig. 7. (a) Calculated temperature-dependent bandgap of the three $Hg_{1-x}Cd_xTe$ films using the expression from [61]. (b) Extracted temperature-dependent equilibrium carrier density from the Drude fits to the THz-TDS measurements for the three $Hg_{1-x}Cd_xTe$ films. The $x = 0.20$ film below 80 K has no data points because no significant free carriers were observed in the spectrum bandwidth. Plotted as lines for the $x = 0.22$ and $x = 0.18$ films is a fit of the carrier density using (6). The $x = 0.20$ line represents the carrier density using (6) for an assumed $N_d = 2 \times 10^{14}$ cm^{-3}. (c) Extracted temperature-dependent effective mass m^* for the three films normalized to the free electron mass m_e. The lines indicate the effective mass m_0^* calculated at the conduction band minimum from [59]. (d) Extracted carrier mobilities $\mu = e\tau/m^*$ from the Drude fits for the three films. The dashed line indicates a $T^{-3/2}$ mobility dependence as a guide to the eye.

are shown in Fig. 7(b)–(d), respectively. The carrier density in Fig. 7(b) exhibits a strong temperature dependence for all three films. At room temperature, all three films have a density over 10^{16} cm^{-3} due to the thermally excited intrinsic carriers. For the $x = 0.22$ and $x = 0.18$ films, the carrier density falls off by an order of magnitude and levels off at low temperatures. This suggests that there is a significant residual background carrier density of order 10^{15} cm^{-3} for the two films, likely from ionized donor impurity states. In narrow-gap $Hg_{1-x}Cd_xTe$, the donor thermal ionization energy is very small (< 1 meV) due to the small conduction band effective mass [50]. Even at low temperatures, where the thermally excited intrinsic carrier density becomes insignificant, we expect considerable donor ionization. Under the assumption of full donor ionization, the total carrier density N seen from our spectroscopy is related to the intrinsic carrier density n_i and ionized donor density N_d by the mass action law [50], [64]

$$n_i^2 = N\,(N - N_d)\,. \tag{6}$$

This expression for N was fit to the experimental data to extract the donor density using a calculated n_i from [51]. The results of the fits are shown as dashed lines over the $x = 0.22$ and $x = 0.18$ data in Fig. 7(b), with extracted doping densities of $N_d = 2.3 \times 10^{15}$ cm^{-3} and $N_d = 1.1 \times 10^{15}$ cm^{-3}, respectively. In contrast, the $x = 0.20$ film density exhibits a strong decrease of nearly two orders of magnitude from 296 to 80 K. Below this temperature, no measurable free-carrier absorption was observed in our bandwidth and no density or mobility could be reasonably determined. Thus, our spectroscopy can only provide an upper bound on the doping of approximately 2×10^{14} cm^{-3} for this film. For the $x = 0.20$ film, we plot the expression for N in (6) using an assumed fixed $N_d = 2 \times 10^{14}$ cm^{-3} to show an upper bound for the donor doping density. At room temperature, all three films have carrier densities in excellent agreement with the expected thermally generated intrinsic density.

The calculated effective masses m^* from our analysis, as shown in Fig. 7(c), are consistently larger than their corresponding band edge values [lines in Fig. 7(c)] for all three films, demonstrating the importance of accounting for nonparabolicity in narrow-gap semiconductors. Straightforward calculations using the band edge mass will result in an overestimate of the mobility and an underestimate of the extracted carrier density. In the future, the effective mass could be more directly probed using a THz magnetospectroscopy setup [15], [16].

Finally, the extracted carrier mobilities are shown in Fig. 7(d). The $x = 0.20$ and $x = 0.18$ films reach very high mobility values exceeding 1×10^5 cm^{2}V^{-1}s^{-1} below 100 K, consistent with Hall measurements of high-quality samples with similar Cd fractions [65], [66]. At temperatures above 80 K, the mobility for all three films is well described by a $T^{-3/2}$ dependence, consistent with phonon scattering dependencies of $T^{-3/2}$ to T^{-2} in $Hg_{1-x}Cd_xTe$ at high temperatures found in the literature [40], [50], [66], [67]. At temperatures below 80 K, the mobility trend in the $x = 0.22$ and $x = 0.18$ films is relatively constant, likely due to the onset of ionized impurity scattering. This is also clearly seen in the reduction of the momentum scattering times at low temperatures in Fig. 5(b). The impurity scattering from the background doping in these two films likely limits the maximum mobility.

Although THz spectroscopy has previously demonstrated good agreement with contacted Hall mobility measurements in semiconductors [68], a comparative study with conventional Hall measurements on $Hg_{1-x}Cd_xTe$ films prepared with

contacts would be necessary in future experiments for validation and implementation in an industrial setting.

IV. Conclusion

In summary, we have used THz-TDS to measure the temperature-dependent complex dielectric function of three epitaxial $Hg_{1-x}Cd_xTe$ films and a bare $Cd_{0.96}Zn_{0.04}Te$ substrate. For the $Hg_{1-x}Cd_xTe$ films, we extracted the electron carrier density, effective mass, momentum scattering time, and mobility as a function of temperature from 296 to 25 K. We found ultrahigh mobilities greater than 1×10^5 $cm^2V^{-1}s^{-1}$ below 100 K in two of the samples ($x = 0.18, 0.20$) and donor densities of 2.3×10^{15} cm^{-3} ($x = 0.22$), 1.1×10^{15} cm^{-3} ($x = 0.18$), and less than 2×10^{14} cm^{-3} in the $x = 0.20$ film, an indication of high-quality epitaxially grown films. This result highlights the use of THz-TDS as a tool to characterize the carrier density and mobility of grown $Hg_{1-x}Cd_xTe$ thin films in a noncontact manner and demonstrates the potential of THz-TDS for noncontact testing of $Hg_{1-x}Cd_xTe$ performance and full-wafer mapping of carrier mobilities.

Acknowledgment

The authors would like to thank G. Popowich, M. Gill, and J. Chaulk for their technical assistance.

References

[1] W. Lei, J. Antoszewski, and L. Faraone, "Progress, challenges, and opportunities for HgCdTe infrared materials and detectors," *Appl. Phys. Rev.*, vol. 2, no. 4, Dec. 2015, Art. no. 041303, doi: 10.1063/1.4936577.

[2] A. Rogalski, "HgCdTe infrared detector material: History, status, and Outlook," *Rep. Prog. Phys.*, vol. 68, no. 10, pp. 2267–2336, 2005, doi: 10.1088/0034-4885/68/10/R01.

[3] C. E. Jones, M. E. Boyd, W. H. Konkel, S. Perkowitz, and R. Braunstein, "Noncontact electrical characterization of epitaxial HgCdTe," *J. Vac. Sci. Technol. A*, vol. 4, no. 4, pp. 2056–2060, Jul. 1986, doi: 10.1116/1.574026.

[4] D. Edwall, J. Phillips, D. Lee, and J. Arias, "Composition control of long wavelength MBE HgCdTe using in-situ spectroscopic ellipsometry," *J. Electron. Mater.*, vol. 30, no. 6, pp. 643–646, Jun. 2001, doi: 10.1007/BF02665849.

[5] K. Moazzami et al., "Detailed study of above bandgap optical absorption in HgCdTe," *J. Electron. Mater.*, vol. 34, no. 6, pp. 773–778, Jun. 2005, doi: 10.1007/s11664-005-0019-3.

[6] T. R. Schimert et al., "Noncontact lifetime characterization technique for LWIR HgCdTe using transient millimeter-wave reflectance," *Proc. SPIE*, vol. 1484, pp. 19–30, Aug. 1991, doi: 10.1117/12.46503.

[7] A. J. Brouns et al., "Non-contact lifetime screening technique for HgCdTe using transient millimetre-wave reflectance," *Semicond. Sci. Technol.*, vol. 8, no. 6S, Jun. 1993, Art. no. 928, doi: 10.1088/0268-1242/8/6S/013.

[8] B. Li et al., "Free-carrier absorption of $Hg_{1-x}Cd_xTe$ epitaxial films," *J. Appl. Phys.*, vol. 79, no. 10, pp. 7738–7742, May 1996, doi: 10.1063/1.362342.

[9] J. Cebulski et al., "Far-infrared reflectivity as a probe of point defects in Zn- and Cd-doped HgTe," *Appl. Phys. Lett.*, vol. 92, no. 12, Mar. 2008, Art. no. 121904, doi: 10.1063/1.2902175.

[10] Y. Chang et al., "Near-bandgap infrared absorption properties of HgCdTe," *J. Electron. Mater.*, vol. 33, no. 6, pp. 709–713, Jun. 2004, doi: 10.1007/s11664-004-0070-5.

[11] J. H. Chu and S. C. Shen, "The study of far-infrared phonon spectra on $Hg_{1-x}Cd_xTe$," *Semicond. Sci. Technol.*, vol. 8, pp. 86–89, 1993, doi: 10.1088/0268-1242/8/1S/019.

[12] P. M. Amirtharaj, N. K. Dhar, J. Baars, and H. Seelewind, "Investigation of phonons in HgCdTe using Raman scattering and far-infrared reflectivity," *Semicond. Sci. Technol.*, vol. 5, no. 3S, pp. S68–S72, Mar. 1990, doi: 10.1088/0268-1242/5/3S/015.

[13] P. U. Jepsen, D. G. Cooke, and M. Koch, "Terahertz spectroscopy and imaging—Modern techniques and applications," *Laser Photon. Rev.*, vol. 5, no. 1, pp. 124–166, 2011, doi: 10.1002/lpor.201000011.

[14] P. Y. Han et al., "A direct comparison between terahertz time-domain spectroscopy and far-infrared Fourier transform spectroscopy," *J. Appl. Phys.*, vol. 89, no. 4, pp. 2357–2359, Feb. 2001, doi: 10.1063/1.1343522.

[15] C. Q. Xia et al., "Hot electron cooling in InSb probed by ultrafast time-resolved terahertz cyclotron resonance," *Phys. Rev. B*, vol. 103, no. 24, 2021, Art. no. 245205, doi: 10.1103/PhysRevB.103.245205.

[16] N. Armakavicius et al., "Electron effective mass in GaN revisited: New insights from terahertz and mid-infrared optical Hall effect," *APL Mater.*, vol. 12, no. 2, 2024, Art. no. 021114, doi: 10.1063/5.0176188.

[17] V. C. Agulto et al., "Terahertz time-domain ellipsometry with high precision for the evaluation of GaN crystals with carrier densities up to 10^{20} cm^{-3}," *Sci. Rep.*, vol. 11, no. 1, 2021, Art. no. 18129, doi: 10.1038/s41598-021-97253-z.

[18] X. Chen and E. Pickwell-MacPherson, "An introduction to terahertz time-domain spectroscopic ellipsometry," *APL Photon.*, vol. 7, no. 7, 2022, Art. no. 071101, doi: 10.1063/5.0094056.

[19] A. Krotkus, R. Adomavičius, and V. Pačebutas, "Characterizing semiconductor materials with terahertz radiation pulses," in *Proc. 6th Int. Conf. Adv. Opt. Mater. Devices*, 2008, vol. 7142, no. 2, pp. 38–49, doi: 10.1117/12.816869.

[20] N. B. Refvik et al., "Ultra-high mobility and temperature-dependent carrier dynamics in narrow-gap $Hg_{1-x}Cd_xTe$ films," in *Proc. 47th Int. Conf. Infrared, Millimeter Terahertz Waves*, 2022, pp. 1–2, doi: 10.1109/IRMMW-THz50927.2022.9895893.

[21] A. Krotkus, R. Adomavičius, G. Molis, A. Urbanowicz, and H. Eusebe, "Terahertz radiation from $Cd_xHg_{1-x}Te$ photoexcited by femtosecond laser pulses," *J. Appl. Phys.*, vol. 96, no. 7, pp. 4006–4008, Oct. 2004, doi: 10.1063/1.1787133.

[22] R. Mendis, M. L. Smith, R. E. M. Vickers, R. A. Lewis, and C. Zhang, "THz emission from mercury cadmium telluride films grown on cadmium zinc telluride substrates," in *Proc. Joint 31st Int. Conf. Infrared Millimeter Waves/14th Int. Conf. Terahertz Electron.*, 2006, pp. 434–434, doi: 10.1109/ICIMW.2006.368642.

[23] G. Molis, R. Adomavičius, and A. Krotkus, "Temperature-dependent terahertz radiation from the surfaces of narrow-gap semiconductors illuminated by femtosecond laser pulses," *Physica B, Condens. Matter*, vol. 403, no. 19/20, pp. 3786–3788, Oct. 2008, doi: 10.1016/j.physb.2008.07.005.

[24] S. Ruffenach et al., "HgCdTe-based heterostructures for terahertz photonics," *APL Mater.*, vol. 5, no. 3, Mar. 2017, Art. no. 035503, doi: 10.1063/1.4977781.

[25] D. B. But et al., "Suppressed auger scattering and tunable light emission of Landau-quantized massless Kane electrons," *Nature Photon.*, vol. 13, no. 11, pp. 783–787, Nov. 2019, doi: 10.1038/s41566-019-0496-1.

[26] K. Kapralov, G. Alymov, D. Svintsov, and A. Dubinov, "Feasibility of surface plasmon lasing in HgTe quantum wells with population inversion," *J. Phys., Condens. Matter*, vol. 32, no. 6, Oct. 2019, Art. no. 065301, doi: 10.1088/1361-648X/ab4f33.

[27] S. V. Morozov et al., "Coherent emission in the vicinity of 10 THz due to auger-suppressed recombination of Dirac Fermions in HgCdTe quantum wells," *ACS Photon.*, vol. 8, no. 12, pp. 3526–3535, Dec. 2021, doi: 10.1021/acsphotonics.1c01111.

[28] V. Y. Aleshkin, A. A. Dubinov, V. I. Gavrilenko, and F. Teppe, "Stimulated emission of plasmon-LO mode in narrow gap HgTe/CdHgTe quantum wells," *J. Opt.*, vol. 23, no. 11, Sep. 2021, Art. no. 115001, doi: 10.1088/2040-8986/ac253d.

[29] S. Dvoretsky et al., "Growth of HgTe quantum wells for IR to THz detectors," *J. Electron. Mater.*, vol. 39, no. 7, pp. 918–923, Jul. 2010, doi: 10.1007/s11664-010-1191-7.

[30] V. V. Rumyantsev et al., "Spectra and kinetics of THz photoconductivity in narrow-gap $Hg_{1-x}Cd_xTe$ ($x < 0.2$) epitaxial films," *Semicond. Sci. Technol.*, vol. 28, no. 12, Oct. 2013, Art. no. 125007, doi: 10.1088/0268-1242/28/12/125007.

[31] D. Yavorskiy et al., "Magnetoconductivity and terahertz response of a HgCdTe epitaxial layer," *Sensors*, vol. 18, no. 12, Dec. 2018, Art. no. 4341, doi: 10.3390/s18124341.

[32] R. Wang et al., "Growth and terahertz characterization of $Hg_{1-x}Cd_xTe$ crystal," *J. Infrared Millimeter Waves*, vol. 30, no. 5, pp. 401–405, 2011.

[33] R. Wang et al., "Terahertz time-domain spectroscopy of $Cd_{1-x}Zn_xTe$ single crystal," in *Proc. 6th Int. Symp. Adv. Opt. Manuf. Testing Technol., Optoelectron. Mater. Devices Sens., Imag., Sol. Energy*, 2012, Art. no. 84190L, doi: 10.1117/12.952479.

[34] J. D. Buron et al., "Terahertz wafer-scale mobility mapping of graphene on insulating substrates without a gate," *Opt. Exp.*, vol. 23, no. 24, pp. 30721–30729, Nov. 2015, doi: 10.1364/OE.23.030721.

[35] C. Zoth et al., "Quantum oscillations of photocurrents in HgTe quantum wells with Dirac and parabolic dispersions," *Phys. Rev. B*, vol. 90, no. 20, Nov. 2014, Art. no. 205415, doi: 10.1103/PhysRevB.90.205415.

[36] C. Stellmach et al., "Time- and spectrally resolved terahertz photoconductivity of quantum Hall systems," *Phys. Rev. B*, vol. 76, no. 3, Jul. 2007, Art. no. 035341, doi: 10.1103/PhysRevB.76.035341.

[37] M. Orlita et al., "Observation of three-dimensional massless Kane Fermions in a zinc-blende crystal," *Nature Phys.*, vol. 10, no. 3, pp. 233–238, Mar. 2014, doi: 10.1038/nphys2857.

[38] F. Teppe et al., "Temperature-driven massless Kane Fermions in HgCdTe crystals," *Nature Commun.*, vol. 7, no. 1, Aug. 2016, Art. no. 12576, doi: 10.1038/ncomms12576.

[39] M. Marcinkiewicz et al., "Temperature-driven single-valley Dirac Fermions in HgTe quantum wells," *Phys. Rev. B*, vol. 96, no. 3, Jul. 2017, Art. no. 035405, doi: 10.1103/PhysRevB.96.035405.

[40] P. Capper and J. Garland, *Mercury Cadmium Telluride: Growth, Properties and Applications*. Hoboken, NJ, USA: Wiley, 2010, ch. 4, doi: 10.1002/9780470669464.

[41] D. N. Purschke et al., "Ultrafast photoconductivity and terahertz vibrational dynamics in double-helix SnIP nanowires," *Adv. Mater.*, vol. 33, no. 34, Aug. 2021, Art. no. 2100978, doi: 10.1002/adma.202100978.

[42] T. L. Cocker et al., "Terahertz conductivity of the metal-insulator transition in a nanogranular VO_2 film," *Appl. Phys. Lett.*, vol. 97, no. 22, Nov. 2010, Art. no. 221905, doi: 10.1063/1.3518482.

[43] M. Schall, M. Walther, and P. U. Jepsen, "Fundamental and second-order phonon processes in CdTe and ZnTe," *Phys. Rev. B*, vol. 64, no. 9, 2001, Art. no. 094301, doi: 10.1103/PhysRevB.64.094301.

[44] J. Neu and C. A. Schmuttenmaer, "Tutorial: An introduction to terahertz time domain spectroscopy (THz-TDS)," *J. Appl. Phys.*, vol. 124, no. 23, Dec. 2018, Art. no. 231101, doi: 10.1063/1.5047659.

[45] M. Walther et al., "Terahertz conductivity of thin gold films at the metal-insulator percolation transition," *Phys. Rev. B*, vol. 76, no. 12, Sep. 2007, Art. no. 125408, doi: 10.1103/PhysRevB.76.125408.

[46] M. Tinkham, "Energy gap interpretation of experiments on infrared transmission through superconducting films," *Phys. Rev.*, vol. 104, no. 3, pp. 845–846, Nov. 1956, doi: 10.1103/PhysRev.104.845.

[47] R. C. Rumpf, "Improved formulation of scattering matrices for semi-analytical methods that is consistent with convention," *Prog. Electromagn. Res.*, vol. 35, pp. 241–261, 2011, doi: 10.2528/PIERB11083107.

[48] L. Thamizhmani, A. K. Azad, J. Dai, and W. Zhang, "Far-infrared optical and dielectric response of ZnS measured by terahertz time-domain spectroscopy," *Appl. Phys. Lett.*, vol. 86, no. 13, Mar. 2005, Art. no. 131111, doi: 10.1063/1.1896451.

[49] L. Wei et al., "Far-infrared quasi-local modes of ZnTe in CdTe," *Solid State Commun.*, vol. 64, no. 8, pp. 1167–1169, Nov. 1987, doi: 10.1016/0038-1098(87)90612-0.

[50] J. Chu and A. Sher, *Physics and Properties of Narrow Gap Semiconductors*. New York, NY, USA: Springer, 2008, pp. 385–557, ch. 5/6, doi: 10.1007/978-0-387-74801-6.

[51] G. L. Hansen and J. L. Schmit, "Calculation of intrinsic carrier concentration in $Hg_{1-x}Cd_xTe$," *J. Appl. Phys.*, vol. 54, no. 3, pp. 1639–1640, Jun. 1983, doi: 10.1063/1.332153.

[52] M. C. Beard, G. M. Turner, and C. A. Schmuttenmaer, "Transient photoconductivity in GaAs as measured by time-resolved terahertz spectroscopy," *Phys. Rev. B*, vol. 62, no. 23, pp. 15764–15777, 2000, doi: 10.1103/PhysRevB.62.15764.

[53] Z. Mics, A. D'Angio, S. A. Jensen, M. Bonn, and D. Turchinovich, "Density-dependent electron scattering in photoexcited GaAs in strongly diffusive regime," *Appl. Phys. Lett.*, vol. 102, no. 23, 2013, Art. no. 231120, doi: 10.1063/1.4810756.

[54] S. C. Howells and L. A. Schlie, "Transient terahertz reflection spectroscopy of undoped InSb from 0.1 to 1.1 THz," *Appl. Phys. Lett.*, vol. 69, no. 4, pp. 550–552, 1996, doi: 10.1063/1.117783.

[55] M. Woźny, J. Cebulski, A. Marcelli, M. Piccinini, and E. M. Sheregii, "Influence of the electron-phonon interaction on the temperature dependence of the phonon mode frequency in the II-VI compound solid solutions," *J. Appl. Phys.*, vol. 117, no. 2, Jan. 2015, Art. no. 025702, doi: 10.1063/1.4905293.

[56] B. Li et al., "Direct observation of vibrational modes in $Hg_{1-x}Cd_xTe$," *Appl. Phys. Lett.*, vol. 68, 1995, Art. no. 3272, doi: 10.1063/1.116571.

[57] M. Lundstrom, *Fundamentals of Carrier Transport*, 2nd ed. Cambridge, U.K.: Cambridge Univ. Press, 2000, ch. 2, doi: 10.1017/CBO9780511618611.

[58] W. Zawadzki, "Electron transport phenomena in small-gap semiconductors," *Adv. Phys.*, vol. 23, no. 3, pp. 435–522, 1974, doi: 10.1080/00018737400101371.

[59] M. H. Weiler, "Magnetooptical properties of Hg1-xCdxTe alloys," *Semicond. Semimetals*, vol. 16, pp. 119–191, 1981, doi: 10.1016/S0080-8784(08)60130-1.

[60] E. O. Kane, "Band structure of indium antimonide," *J. Phys. Chem. Solids*, vol. 1, no. 4, pp. 249–261, Jan. 1957, doi: 10.1016/0022-3697(57)90013-6.

[61] G. L. Hansen, J. L. Schmit, and T. N. Caselman, "Energy gap versus alloy composition and temperature in $Hg_{1-x}Cd_xTe$," *J. Appl. Phys.*, vol. 53, pp. 7099–7101, 1982, doi: 10.1063/1.330018.

[62] N. Ashcroft and N. D. Mermin, *Solid State Physics*. Philadelphia, PA, USA: Saunders College, 1976.

[63] Y. Chang et al., "Absorption of narrow-gap HgCdTe near the band edge including nonparabolicity and the Urbach tail," *J. Electron. Mater.*, vol. 36, no. 8, pp. 1000–1006, Aug. 2007, doi: 10.1007/s11664-007-0162-0.

[64] S. M. Sze, Y. Li, and K. K. Ng, *Physics of Semiconductor Devices*, 4th ed. Hoboken, NJ, USA: Wiley, 2021, ch. 1, sec. 4, doi: 10.1002/0470068329.

[65] R. Dornhaus and G. Nimtz, "The properties and applications of the Hg1-xCdxTe alloy system," in *Narrow-Gap Semiconductors*. Berlin, Germany: Springer, 1983, pp. 119–281, doi: 10.1007/BFb0044919.

[66] J. P. Rosbeck, R. E. Starr, S. L. Price, and K. J. Riley, "Background and temperature dependent current-voltage characteristics of HgCdTe photodiodes," *J. Appl. Phys.*, vol. 53, no. 9, Aug. 1998, Art. no. 6430, doi: 10.1063/1.331516.

[67] J. Antoszewski and L. Faraone, "Analysis of magnetic field dependent Hall data in narrow bandgap $Hg_{1-x}Cd_xTe$ grown by molecular beam epitaxy," *J. Appl. Phys.*, vol. 80, no. 7, pp. 3881–3892, Oct. 1996, doi: 10.1063/1.363344.

[68] B. G. Alberding, W. R. Thurber, and E. J. Heilweil, "Direct comparison of time-resolved terahertz spectroscopy and Hall Van der Pauw methods for measurement of carrier conductivity and mobility in bulk semiconductors," *J. Opt. Soc. Amer. B*, vol. 34, no. 7, pp. 1392–1406, Jul. 2017, doi: 10.1364/JOSAB.34.001392.